LAWRENCE
LIVERMORE
NATIONAL
LABORATORY

LLNL-JRNL-748566

Adaptive mesh refinement in stress-constrained topology optimization.

M. A. Salazar de Troya, D. A. Tortorelli

March 26, 2018

Structural and Multidisciplinary Optimization

Disclaimer

LLNL-JRNL-748566

Adaptive mesh refinement in stress-constrained topology optimization

Miguel A. Salazar de Troya, Daniel A. Tortorelli

the date of receipt and acceptance should be inserted later

Abstract We present a topology structural optimization framework with adaptive mesh refinement and stress-constraints. Finite element approximation and geometry representation benefit from such refinement by enabling more accurate stress field predictions and greater resolution of the optimal structural boundaries. We combine a volume fraction filter to impose a minimum design feature size, the RAMP penalization to generate "black-and-white designs" and a RAMP-like stress definition to resolve the "stress singularity problem". Regions with stress concentrations dominate the optimized design. As such, rigorous simulations are required to accurately approximate the stress field. To achieve this goal, we invoke a threshold operation and mesh refinement during the optimization. We do so in an optimal fashion, by applying adaptive mesh refinement techniques that use error indicators to refine and coarsen the mesh as needed. In this way, we obtain more accurate simulations and greater resolution of the design domain. We present results in two dimensions to demonstrate the efficiency of our method.

Keywords Topology Optimization · Stress Constrained · Adaptive Mesh Refinement

1 Introduction

Topology optimization is a well established design tool that has found industrial applications in recent years. However, most developments focus on the "compliance problem", i.e. to minimize compliance subject to a mass constraint. This is in spite of the fact that in many cases, it is necessary to satisfy failure constraints such as on maximum yield stress. In this work, we investigate stress constrained topology optimization.

There are numerous challenges to solve stress-constrained problems. First, the optimal stress constrained solutions belong to degenerate lower dimension subspaces of the design domain. Gradient-based optimization algorithms cannot reach these optima; rather they get trapped in locally optimal solutions. This phenomenon, first studied in the optimal design of trusses Sved and Ginos (1968); Kirsch (1990); Cheng and Jiang (1992) is known in the literature as the "singularity problem". It is resolved by relaxing the stress constraints, thereby regularizing the degenerate subspace Rozvany and Birker (1994); Cheng and Guo (1995) . This is accomplished via $\varepsilon-relaxation$ Cheng and Guo (1997) or $qp-relaxation$ Bruggi (2008) and the relaxed stress indicator Le et al (2010). In this work, we employ the last.

Second, the local stress constraints in the continuum setting lead to one constraint per finite element after discretization. This creates a scenario where the number of design variables is as large as the number of constraints, which is a computationally challenging problem. To overcome this, the constraints are agglomerated into a single measure that approximates the maximum stress value over the domain. These approximations include the p-norm and the Kreisselmeier-Steinhauser (KS) functions Park (1995). Alternatively, in Amstutz and Novotny (2010) a ramp function is used to penalize all regions with stress constraint violations. We adopt this approach.

M. Salazar de Troya · D. Tortorelli
Lawrence Livermore National Laboratory
Livermore, CA, USA

University of Illinois at Urbana-Champaign
Champaign-Urbana, IL, USA
E-mail: salazardetro1@llnl.gov

Third, the inaccuracy of the computed stress field leads to designs that do not perform in service as their simulations suggest. This is because topology optimization does not use a conforming mesh; rather, it projects the design onto a fixed grid akin to a fictitious domain finite element method. Although this approach is convenient for the optimization, it yields poor accuracy in the computed response. This issue is exasperated in density-based topology optimization because the domain geometry is not explicitly defined; rather it is defined by an interphase of "partially filled" finite elements which renders useless stress computations. In this work, we use Adaptive Mesh Refinement (AMR) and thresholding to obtain accurate stress values. Our goals are to obtain comparable optimal designs to those that are obtained on highly refined uniform meshes, compute accurate stress fields and reduce the computational cost. To achieve these goals we need a reliable and efficient error indicator to drive the AMR and a topology optimization strategy that accommodates the evolving discretization.

The first application of AMR in topology optimization appears in Maute and Ramm (1995); it uses separate design and analysis meshes which are related by a smoothing algorithm. The AMR is only performed on the analysis mesh; it is based on geometric criteria and no coarsening is performed. Coarsening is considered in Wang et al (2010) which uses a mesh hierarchy to solve the compliance problem. Again the refinement and coarsening criteria are solely based on the geometry and not on the error in the computed response. A similar approach proposed in Nana et al (2016) uses the distance function with respect to the domain boundary as the refinement and coarsening indicator. A study of the effects of various AMR parameters on the optimization performance appears in Panesar et al (2017). As in Maute and Ramm (1995), they use different design and analysis meshes and as in Nana et al (2016), the AMR uses a geometric error indicator that is based on the proximity to the domain boundary. In Nguyen-Xuan (2017), the AMR uses a tree data structure with polygonal elements; again the error indicator is solely based on geometrical considerations. Following this trend, Stainko (2006) uses the phase-field method and refines regions adjacent to the design boundary.

Independently discretizing the design and analysis meshes, Wang et al (2014) refines each with their own error indicators to solve the compliance problem. Unfortunately, this approach is not scalable because it is necessary to perform a search over the design discretization for each finite element in the analysis mesh. On a positive note, a posteriori error estimators are used to obtain accurate displacement and stress fields. In Bruggi and Verani (2011) two different error estimators are invoked to control error in the geometry and compliance. However, their method is only applied to compliance problems. An energy based error indicator is used in Wallin et al (2012) to refine the mesh in the compliance problem. In the context of stress-constrained problems, Costa Jr et al (2005) utilizes h-adaptive mesh refinement by combining mesh quality and displacement based error indicators. However, they do not validate the accuracy of their stress fields. Jensen (2016) solves a stress constrained compliance minimization problem using an anisotropic mesh adaptation scheme based on the metric tensors of the spatial Hessian of the cost and constraint functions. Using topological derivatives Amstutz and Novotny (2010) considers local stress constraints and develops an AMR method that is based on residual error indicators of the energy norm of the displacement.

Finite element analysis in structural topology optimization is a delicate issue, especially in regard to the calculation of the stress fields. Indeed, stress fields are not accurately resolved with the density method due to the blurred boundary region. Because of this, topology optimized designs are post processed wherein the blurred boundary is thresholded to define an "exact" boundary, a conforming mesh is created from this boundary and shape optimization is used to obtain designs with desirable stress distributions. To eliminate the shape optimization task, Svärd (2015) embeds stress field post-processing into the topology optimization wherein the interior stress values are extrapolated to the boundary region to compute more accurate stress fields. Another option to obtain accurate stress fields is to define an explicit domain boundary with the level set method and use either a conforming mesh Lian et al (2017); Allaire et al (2014); Xia et al (2012) or eXtended Finite Element Method (XFEM) and similar approaches Guo et al (2011); Zhang et al (2013); Guo et al (2014); Sharma and Maute (2018) to capture the boundary. However, level-set methods cannot systematically nucleate holes and their designs are highly dependent on the initial design, which limits their effectiveness in comparison to density methods. It is possible to nucleate holes via topological derivatives; however, this approach is only practical for linear problems. It is also well known that level set methods suffer from poor convergence rates and numerical oscillations in the boundary Gain and Paulino (2013). They are also difficult to implement. However, for stress-constrained problems, they are immune to the singularity issue because there is virtually no blurred boundary region.

Our contribution is a topology optimization framework to obtain designs that satisfy pointwise stress constraints with a high degree of accuracy. We are able to achieve this goal by combining AMR and a thresholding function to obtain a sharp interphase that models the material boundary.

We implement our topology optimization framework on top of the parallel finite element library libMesh Kirk et al (2006), which allows us to address large scale problems. This framework accomodates arbitrary cost and constraint functions and can be extended to other physics than elasticity. The high performance capability will be essential when solving problems in three dimensions, which is the scope of our future work.

2 Adaptive mesh refinement in stress-constrained topology optimization

Topology optimization finds the distribution of material within a hold-all domain D that minimizes a cost function and satisfies constraints. Its mathematical statement is as follows

$$\min_{\chi\in\{0,1\}} \theta_0(\chi) = \int_D \pi(\chi,\mathbf{u})\ dV\,, \tag{1}$$

$$\text{s.t. } \mathbf{u}\in V \text{satisfies } a(\chi;\mathbf{u},\mathbf{v}) = L(\mathbf{v}) \text{ for all } \mathbf{v}\in V\,, \tag{2}$$

$$\theta_i(\chi) = \int_D g_i(\chi,\mathbf{u})dV \le 0\ i=1,2...\mathrm{n}_i\,, \tag{3}$$

where

$$a(\chi;\mathbf{u},\mathbf{v}) = \int_D \chi\mathbb{C}[\nabla\mathbf{u}]\cdot\nabla\mathbf{v}\ dV \tag{4}$$

and

$$L(\mathbf{v}) = \int_{\Gamma_N} \mathbf{t}\cdot\mathbf{v}\ da\,. \tag{5}$$

In the above, χ is the material indicator function defined such that $\chi(\mathbf{x})=1$ and $\chi(\mathbf{x})=0$ represents the presence or lack of material at $\mathbf{x}\in D$, θ_0 is the cost function to be minimized, e.g. compliance, mean displacement, maximum stress, etc. and θ_i are the n_i inequality constraint functions that typically limit the total mass, maximum stress, etc. In addition, the design needs to satisfy the linear elasticity equation, given in its weak form in Equation (2) where $\mathbf{u}$ is the displacement field and $V = \left\{\mathbf{v}\in H^1(D)^d \mid \mathbf{v}=\mathbf{0} \text{ on } \Gamma_D\right\}$ is the function space of admissible displacements, where Γ_D is the boundary of D over which Dirichlet boundary conditions $\mathbf{u}=\mathbf{0}$ are applied. Γ_N is the complementary boundary of ∂D over which the non-homogeneous traction $\mathbf{t}$ is applied; both Γ_D and Γ_N are fixed surfaces. Finally, $\mathbb{C}$ is the symmetric elasticity tensor.

Our discrete optimization problem is not amenable to gradient-based algorithms. For this reason, we 1) convexify the design domain by replacing the binary-valued design field $\chi\in\{0,1\}$ with the volume fraction field ν, which continuously varies from 0 to 1, i.e. $\nu\in[\epsilon_\nu,1]$, and 2) penalize intermediate values so that ν best mimics the characteristic function χ. This ensures the elasticity problem is well-posed. In this work, we penalize the elasticity tensor by replacing χ in Equation (4) with the RAMP function Stolpe and Svanberg (2001)

$$r(\nu) = \frac{\nu}{1+q(1-\nu)}\,, \tag{6}$$

where q is the penalization parameter. Figure 1 plots the RAMP function for several values of q. We observe better behavior using the RAMP rather than the traditional SIMP method Bendsøe and Sigmund (1999). We use the usual ersatz material to model regions with no material, i.e., we replace regions where $\chi(\mathbf{x})=0$ with $\nu(\mathbf{x})=\epsilon_\nu$.

Unfortunately, the topology optimization problem is ill-posed. Compliance designs consist of a non converging sequence of structures with highly oscillatory material-void regions. There are two approaches to obtain a well-posed problem, relaxation and restriction. We use the restriction approach, wherein the design space is reduced by imposing a length scale constraint on the design's geometric features. This is accomplished by imposing a constraint on the perimeter Haber et al (1996), the slope of the volume fraction field Petersson and Sigmund (1998) or as in this work, by filtering the volume fraction field Bourdin (2001). In this work, we use the cone filter presented in Bruns and Tortorelli (2001).

$$\hat{\nu}(\mathbf{x},\nu) = \int_{\mathcal{B}_\epsilon(\mathbf{x})} K(\mathbf{x}-\mathbf{y})\nu(\mathbf{y})dV\,, \tag{7}$$

where $\mathcal{B}_\epsilon(\mathbf{x})$ is a ball of radius ϵ centered at $\mathbf{x}$ and $K(\mathbf{x}-\mathbf{y})$ is the cone kernel function, given by

$$K(\mathbf{p}) = \frac{1}{\epsilon}(\epsilon - \|\mathbf{p}\|) \text{ if } \mathbf{p}\in\mathcal{B}_\epsilon(\mathbf{x})\,. \tag{8}$$

The filter radius ϵ is a parameter which defines the length scale such that the geometric complexity increases as $\epsilon\to 0$. It is important to consider the integral in Equation (7) instead of the weighted average of neighboring elements, as commonly seen in the literature, because the elements have different volume/areas when applying AMR. We considered using the PDE-based filter Lazarov and Sigmund (2011), but its solution with traditional lagrange elements requires a sufficiently refined mesh to avoid filtered volume fraction

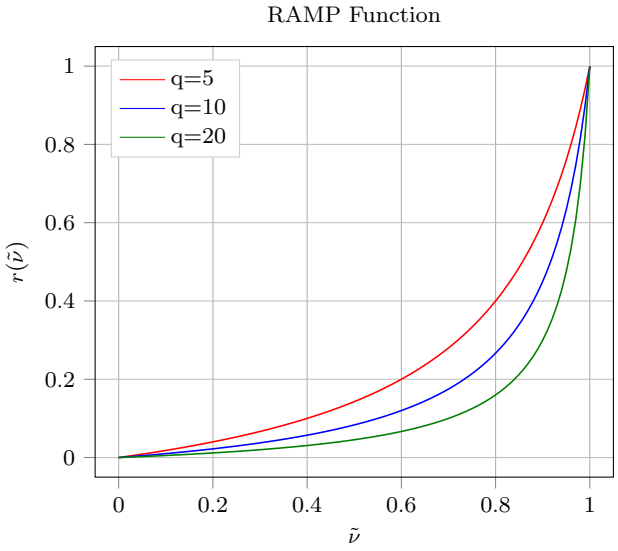

Fig. 1 RAMP interpolation scheme.

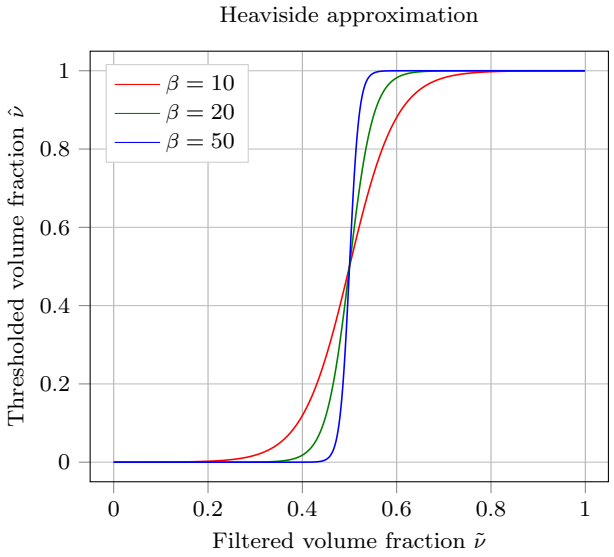

Fig. 2 Threshold function.

values above 1 and below 0. This is not possible at early stages of our AMR strategy. We will investigate in the future alternative methods that avoid this oscillation.

The filter operation brings an additional issue: the presence of blurred boundaries in the material interface. To lessen this effect, we use the threshold function of Wang et al (2011), cf. Equation (9),

$$\tilde{\nu}(\hat{\nu}) = \frac{\tanh(0.5\beta) + \tanh(\beta(\hat{\nu} - 0.5))}{\tanh(0.5\beta) + \tanh(\beta(1.0 - 0.5))}\,, \tag{9}$$

where β is a parameter defined such that

$$\lim_{\beta\to\infty} \tilde{\nu}(\hat{\nu}) = H(x - 0.5)\,, \tag{10}$$

where H is the unit step function. It is known that the threshold operation does not prevent the appearance of localized artifacts such as one-node-connected hinges in compliant problems, which can be alleaviated with a robust formulation Wang et al (2011) or with a stress constraint De Leon et al (2015). Therefore, we do not worry about features below the minimum length scale. The thresholding function makes the sensitivity zero in regions away from the $\tilde{\nu} = 0.5$ level set boundary, which makes it difficult to nucleate holes. For this reason, we use a continuation approach wherein β is selectively increased during the optimization.

Summarizing, we replace the binary material indicator field χ with the continuous volume fraction field ν to convexify the design space and make the optimization problem amenable to NLP. We compute the filtered volume fraction field $\hat{\nu}$ to impose a length scale constraint and hence obtain a well-posed optimization problem. Finally we compute the thresholded volume fraction field $\tilde{\nu}$ such that it mimics the originally sought material indicator function χ. Ultimately we solve the topology optimization problem of finding ν such that

$$\min_{\nu\in[\epsilon_\nu,1]} \theta_0(\nu) = \int_D \pi(\tilde{\nu}, \mathbf{u})\; dV\,, \tag{11}$$

$$\text{s.t. } \mathbf{u} \in V \text{satisfies } a(\nu; \mathbf{u}, \mathbf{v}) = L(\mathbf{v}) \text{ for all } \mathbf{v} \in V\,, \tag{12}$$

$$\theta_i(\nu) = \int_D g_i(\tilde{\nu}, \mathbf{u}) dV \le 0 \;\; i = 1, 2..\mathrm{n}_i\,, \tag{13}$$

where

$$a(\nu; \mathbf{u}, \mathbf{v}) = \int_D r(\tilde{\nu}) \mathbb{C}[\nabla \mathbf{u}] \cdot \nabla \mathbf{v}\; dV\,. \tag{14}$$

3 Stress field accuracy in the density method

Convexifying the design space has the effect of blurring the domain boundaries, which creates inaccurate stress field computations, as demonstrated by Svärd (2015). In their work, sharper boundaries are obtained via a non-linear filter rather than the cone filter of Equation (7). Because of the mesh resolution, however, the boundary is jagged which gives rise to artificially high stress values. To resolve this jaggedness, the stress fields are post-processed by extrapolating the interior values onto the boundary.

In this work, we demonstrate that stress post-processing is not necessary if the mesh is adaptively refined leaving only a fine interphase boundary region. To validate our method, we perform the dog-bone study of Svärd (2015) cf. Figure 3 in which $D = 1\ m$ and $r = 1/3\ m$. The material Young's modulus is $E = 10\ Pa$ and the Poisson ratio, $\mu = 0.3$. The volume fraction

field that defines the plane stress structure is discretized as piecewise constant over the elements. The geometry is directly interpolated onto the mesh, i.e. only the elements whose centroids $\mathbf{x}_i$ are within the structure boundary take a $\nu(\mathbf{x}_i) = 1$ volume fraction. For all other void elements we assign $\nu(\mathbf{x}_i) = \epsilon_\nu = 10^{-5}$. We then filter the volume fraction with Equation (7) and $\epsilon = 0.0625\ m$ and thresholded with Equation (9) using $\beta = 100$ to leave a fine interphase region with intermediate volume fraction values. We apply uniaxial loading of 10 Pa significantly distant from the notches to avoid end effects in the notch region. Our calculated minimum principal stress is compared to those from empirical formulas Young and Budynas (2002). This computation is repeated for several dog-bone orientations within the fixed mesh. In Figure 5, we plot the minimum principal stress across section A-A that passes through the center of the notch where it is seen that stress converges to the same distribution regardless of the orientation. The minimum principal stress value is -39.8, which is similar to the tabulated value -39.02 in Young and Budynas (2002).

To obtain these results, we use the residual based error indicator of Equation (36) and the Dörfler marking strategy Dörfler (1996) which is proven to decrease the error in elliptic problems. Unlike the marking strategy that we will employ in the optimization, the Dörfler strategy does not allow for coarsening. In our Dörfler implementation we select a subset $\mathcal{M}$ of elements with minimum cardinality such that

$$\eta_{\mathcal{M}} = \left(\sum_{K \in \mathcal{M}} \eta_K^2 \right)^{1/2} \geq \theta \eta \quad \theta \in [0, 1]\,, \tag{15}$$

where

$$\eta = \left(\sum_{K \in \mathcal{T}_h} \eta_K^2 \right)^{1/2} \tag{16}$$

and η_K is the element error of Equation (36) and $\theta = 0.3$. The mesh is iteratively refined until the total energy error η of Equation (39) is below 0.5. Figure 4 shows the refined mesh for an orientation of 0.4.

4 Stress constrained topology optimization

Now we are in a position to formulate our topology optimization problem. We intend to minimize the volume of the structure subject to a constraint on the von Mises stress

$$\sigma_{VM} = \sqrt{\frac{3}{2} \boldsymbol{\sigma}^{\boldsymbol{dev}} \cdot \boldsymbol{\sigma}^{\boldsymbol{dev}}}\,, \tag{17}$$

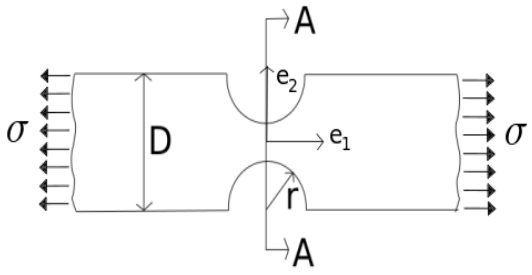

Fig. 3 Dog-bone structure from Young and Budynas (2002).

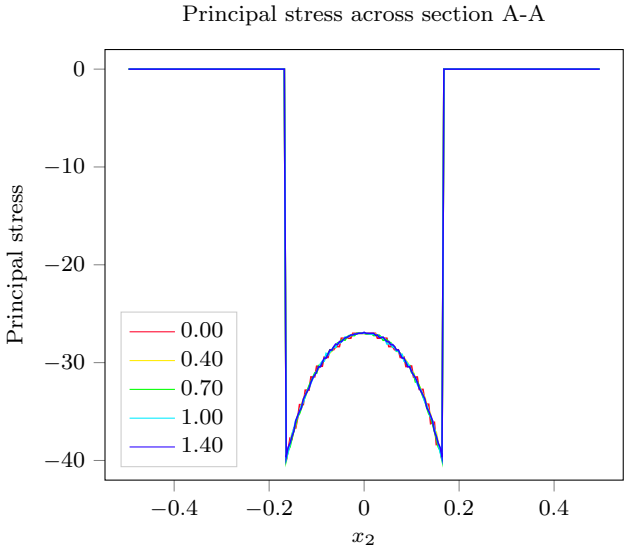

Fig. 5 Minimum principal stress over cross section A-A for orientations 0.0, 0.4, 0.7, 1.0 and 1.4 rad.

where

$$\boldsymbol{\sigma}^{\boldsymbol{dev}} = \boldsymbol{\sigma} - \frac{1}{3}(\mathrm{tr}\boldsymbol{\sigma})\mathbf{I} \tag{18}$$

is the deviatoric stress. As such the topology optimization problem now reads

$$\min_{\nu \in [\epsilon_\nu, 1]} \theta_0(\nu) = \int_D \tilde{\nu}\ dV\,, \tag{19}$$

$$\text{s.t. } \mathbf{u} \in V \text{satisfies } a(\nu; \mathbf{u}, \mathbf{v}) = L(\mathbf{v}) \text{ for all } \mathbf{v} \in V\,, \tag{20}$$

$$\text{and } \theta_1(\nu) = \sigma_{VM} \leq \sigma_y \quad \text{for all } \mathbf{x} \in D\,, \tag{21}$$

where σ_y is the maximum allowed stress.

A consistent numerical approach would use the same elasticity tensor for the displacement solution and the stress evaluation. However, Duysinx and Bendsøe (1998) showed that the stress field in a porous micro structure tends to a non-zero value even when the volume fraction tends to zero. To be physically accurate,

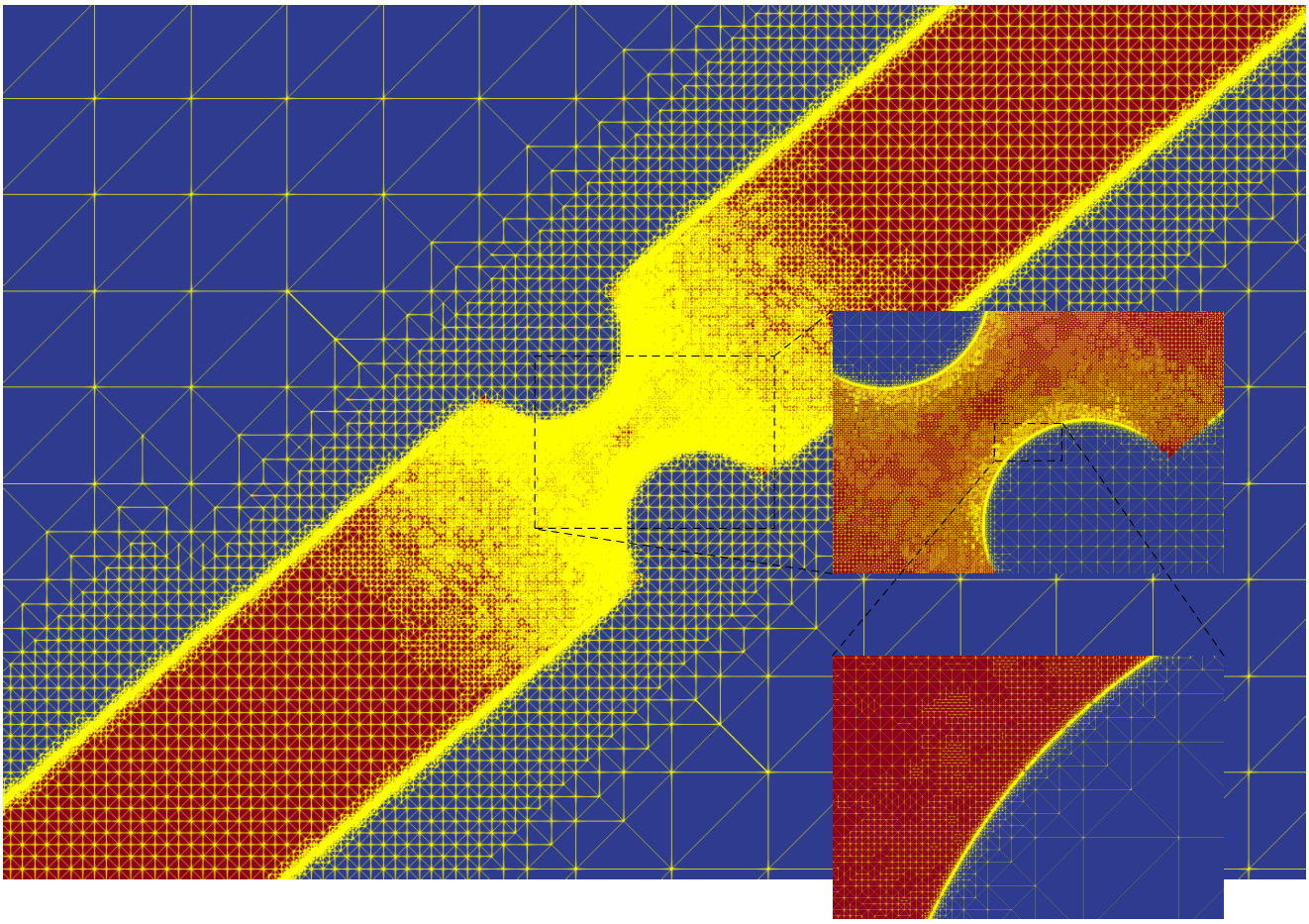

Fig. 4 Dog-bone structure and the mesh used in the analysis for an orientation of 0.4 radians.

the stress field in regions with intermediate volume fraction $\nu \in [\epsilon_\nu, 1]$ should therefore tend to non-zero values as ν tends to zero. However, our focus is in obtaining black-and-white designs so we are not interested in accurately calculating the stress in regions with intermediate volume fraction. Therefore, when computing the stress we use a relaxed stress formulation similar to Le et al (2010) wherein

$$\mathbb{C}(\tilde{\nu}) = \eta_c(\tilde{\nu})\mathbb{C}_0\,, \tag{22}$$

where η_c is the inverse RAMP function

$$\eta_c(\tilde{\nu}) = \tilde{\nu}\frac{1+q}{1+q\tilde{\nu}}\,, \tag{23}$$

cf. Figure 6. Basically, when computing the displacement in regions with intermediate volume fraction, we penalize $\mathbb{C}$ such that it is more compliant which generates a displacement field which is artificially "large". We now combine this large displacement field with a stiff $\mathbb{C}$ to compute an artificially large stress field. Because of the volume minimization, the optimizer deems such regions inefficient and hence reduces their size.

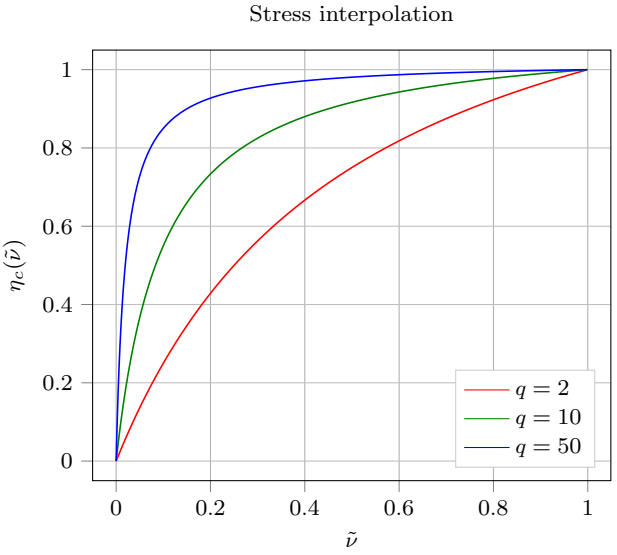

Fig. 6 Stress penalization function.

The stress constraint Equation (21) is a pointwise constraint. When solving the elasticity equation using the finite element method, the pointwise constraint

translates into one constraint per finite element; it is evaluated at the element centroid $\mathbf{x}_i$. This results in a computationally challenging optimization problem. To resolve this burden, the pointwise constraints $\sigma_{VM}(\mathbf{x}_i) \leq \sigma_y$ are replaced by the single global maximum constraint $\max_{\mathbf{x}_i} \sigma_{VM}(\mathbf{x}_i) \leq \sigma_y$. However, this constraint is not differentiable, which hinders the optimization algorithm. As such aggregation strategies in Duysinx and Bendsøe (1998); Yang and Chen (1996) approximate the maximum value of the Von Mises stress field with a p-norm or a Kreisselmeier-Steinhauser (KS) function Guilherme and Fonseca (2007). Obviously the single global measure cannot represent the pointwise field values. To address this shortcoming, several strategies employ regional measures Le et al (2010); París et al (2010); Holmberg et al (2013), where the single agglomerated constraint over the entire domain is replaced by several such constraints over subdomains. Another shortcoming with these aggregated measures is that they only approximate the maximum field value. A renormalization strategy was presented in Le et al (2010) to improve the approximation. However, this approach results in a non-differentiable constraint although the effect of the non-differentiability lessens as the optimization converges.

We apply a different aggregation strategy that is commonly used in PDE-constrained optimization Hintermüller and Hinze (2009) and in Amstutz and Novotny (2010) for stress constrained optimization via the topological derivative. It requires neither renormalization nor regional clustering techniques. We replace the pointwise constraint Equation (21) with the global constraint $\|\sigma_{VM} - \sigma_y\|_+ = \int_D R(\frac{\sigma_{VM}}{\sigma_y}) dV$ where R is the shifted ramp function: $R(x) = x - 1$ if $x > 1$ and $R(x) = 0$ otherwise. For the optimization, we replace the ramp function with a smooth approximation R_p such that

$$R_p(x) = (1 + (x)^p)^{\frac{1}{p}} - 1\,, \tag{24}$$

cf. Figure 7. In our calculations, we use $p = 8$ and leave it constant throughout the optimization.

The constraint of Equation (24) is enforced via a penalty method with a penalty parameter γ so that the topology optimization problem now reads

$$\min_{\nu \in (0,1]} \theta_0(\nu) = \int_D \tilde{\nu}\; dV + \gamma \left\|\sigma_{VM} - \sigma_y\right\|_+\,, \tag{25}$$

$$\text{s.t. } \mathbf{u} \in V \text{satisfies } a(\nu; \mathbf{u}, \mathbf{v}) = L(\mathbf{v}) \text{ for all } \mathbf{v} \in V\,. \tag{26}$$

The parameter γ is increased throughout the optimization, starting from a small value. This helps alleviate the sharp gradient in Equation (24).

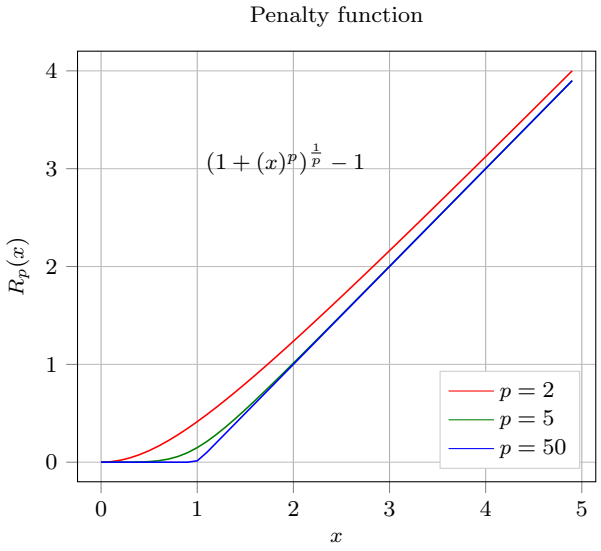

Fig. 7 Smoothed shifted function.

We use an adjoint sensitivity analysis to evaluate the variation of a general functional $\theta(\nu)$. Although this derivation is well-known, it behooves us to present it as it also plays a role in our AMR.

We use a reduced space optimization formulation, hence we must consider dependency of $\mathbf{u}$ on the design variable ν, i.e. $\mathbf{u} \to \mathbf{u}(\nu)$ so that $\hat{\theta}(\nu) = \theta(\nu, \mathbf{u}(\nu))$. In this way

$$\delta\hat{\theta}(\nu; \delta\nu) = \delta_\nu \theta(\nu, \mathbf{u}(\nu); \delta\nu) + \delta_{\mathbf{u}} \theta(\nu, \mathbf{u}(\nu); \delta\mathbf{u}(\nu; \delta\nu))\,, \tag{27}$$

where $\delta\hat{\theta}(\nu; \delta\nu)$ is the variation of $\hat{\theta}$ at ν acting on $\delta\nu$; $\delta_{\mathbf{u}}\theta$ is the variation of θ at $\mathbf{u}$ acting on $\delta\mathbf{u}$, $\delta_\nu\theta$ is the variation of θ at ν acting on $\delta\nu$ and $\delta\mathbf{u}$ is the variation of $\mathbf{u}$ at ν acting on $\delta\nu$. In the adjoint method, we annihilate the implicit variation $\delta\mathbf{u}(\nu; \delta\nu)$. To do this we take the variation of the state Equation (26) with respect to the design field ν and augment this zero term to $\delta\hat{\theta}$.

$$\begin{aligned}
\delta\hat{\theta}(\nu; \delta\nu) &= \delta_\nu \theta(\nu, \mathbf{u}(\nu); \delta\nu) && (28)\\
&\quad + \delta_{\mathbf{u}} \theta(\nu, \mathbf{u}(\nu); \delta\mathbf{u}(\nu; \delta\nu)) && (29)\\
&\quad - \delta_\nu a(\mathbf{u}, \mathbf{v}; \delta\nu) && (30)\\
&\quad - \delta_{\mathbf{u}} a(\mathbf{u}, \mathbf{v}; \delta\mathbf{u}(\nu; \delta\nu))\,, && (31)
\end{aligned}$$

where $\delta_\nu a$ and $\delta_{\mathbf{u}} a$ are the variations of the bilinear form a with respect to ν and $\mathbf{u}$. In our linear elasticity formulation

$$\delta_{\mathbf{u}} a(\mathbf{u}, \mathbf{v}; \delta\mathbf{u}(\nu; \delta\nu)) = a(\mathbf{v}, \delta\mathbf{u}(\nu; \delta\nu))\,, \tag{32}$$

and

$$\delta_\nu a(\mathbf{u}, \mathbf{v}; \delta\mathbf{u}(\nu; \delta\nu)) = \int_D \delta r(\tilde{\nu}; \delta\tilde{\nu}(\nu; \delta\nu)) \mathbb{C}[\nabla\mathbf{u}] \cdot \nabla\mathbf{v}\; dV\,. \tag{33}$$

To annihilate $\delta\mathbf{u}(\nu;\delta\nu)$ in Equation (31), we define the arbitrary $\mathbf{v} \in V$ such that

$$a(\mathbf{v},\delta\mathbf{u}) = \delta_{\mathbf{u}}\theta(\nu,\mathbf{u}(\nu);\delta\mathbf{u}) \text{ for all } \delta\mathbf{u} \in V\,, \tag{34}$$

where we use the symmetry of the bilinear from a. Having calculated $\mathbf{v}$, $\delta\hat{\theta}$ reduces to.

$$\delta\hat{\theta}(\nu;\delta\nu) = \delta_{\nu}\theta(\nu,\mathbf{u}(\nu);\delta\nu) - \delta_{\nu}a(\mathbf{u},\mathbf{v},\delta\nu)\,. \tag{35}$$

Summarizing, to calculate $\delta\hat{\theta}(\nu)$, we first solve the primal problem of Equation (26) to obtain $\mathbf{u}$, we compute the partial derivative information $\delta_{\mathbf{u}}\theta(\nu,\mathbf{u}(\nu);\delta\mathbf{u})$ and $\delta_{\nu}\theta(\nu,\mathbf{u}(\nu);\delta\nu)$, we solve the adjoint problem of Equation (34) for $\mathbf{v}$ and finally we compute the variation $\delta\hat{\theta}$ from Equation (35).

4.1 Adaptive mesh refinement

To produce meaningful designs, we must compute the stress field with as much accuracy and efficiency as possible, hence the motivation to use AMR. More importantly, in optimization, AMR also provides an accurate and efficient means to compute the cost and constraint functions. Indeed, the engineer is basing the entire design on the values of these functions so their computed values must be accurate.

The accuracy of our finite element computation is directly dependent on the spatial discretization. To gauge this accuracy we compute an error measure which allows us to best allocate the spatial discretization parameters while simultaneously achieving the desired accuracy. In the context of finite element methods, these measures are called a posteriori error estimates. They bound the error in terms of the current solution approximation and are computed by summing the element error indicators over the mesh. In our h-refinement AMR strategy, a marking strategy identifies the elements with largest and smallest errors for refinement and coarsening. The elements to be refined are divided in four children elements, which belong to a different refinement level, cf. Figure 8. Those elements to be coarsened are removed along with the corresponding children from the same parent, cf. Figure 9. The refinement creates so called "hanging nodes" that break the continuity of the displacement field. To ensure continuity, constraints are imposed that relate these nodes' displacements to their parents'. We only allow for hanging nodes between children and their parents neighbors; i.e. not between children and their grandparents neighbors. Such situations are corrected by adding more elements, cf. Figure 10.

As just mentioned, the AMR strategy relies on element error indicators. The theory of a posteriori finite element error estimation for elliptic problems is well established cf. the monographs Ainsworth and Oden (2011); Verfürth (2013). The a posteriori error estimates are categorized into three types: explicit residual-based error estimates, implicit residual-based error estimates and gradient or flux recovery based error estimates. The explicit and implicit methods approximate the error with the current finite element solution. The explicit estimates are easy to implement, however they render bounds with problem dependent constants that can be difficult to assign. The implicit estimates require the solution of multiple regional boundary value problems over single elements or small element patches. The

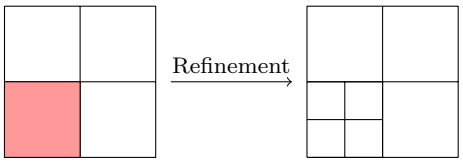

Fig. 8 Element marked for refinement in red and the resulting refinement with now two levels.

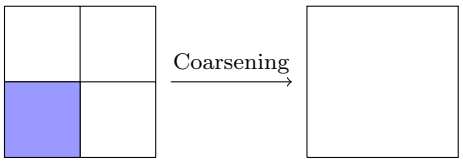

Fig. 9 Element marked for coarsening in blue and the coarsening result.

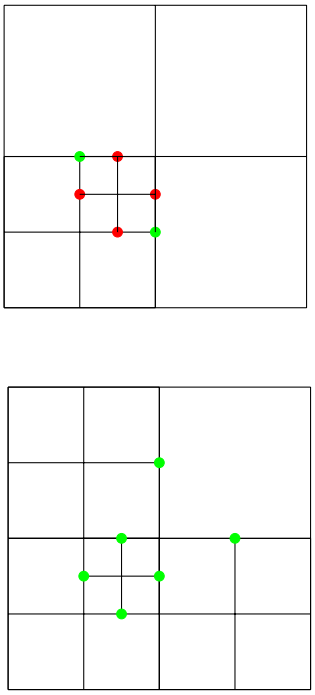

Fig. 10 Allowed hanging nodes green and disallowed hanging nodes in red (top) and additional refinement to resolve disallowed hanging nodes (bottom).

problem dependent constants are avoided at the behest of additional computational expense and onerous implementations. Error estimates based on gradient or flux recovery post-process the finite element displacement field $\mathbf{u}_h$ to obtain an improved approximation of the stress field $\hat{\boldsymbol{\sigma}}(\mathbf{u}_h)$ which is smooth and has better convergence properties versus the nominally computed discontinuous stress field $\boldsymbol{\sigma}(\mathbf{u}_h)$. The element error indicator is based on the difference between $\hat{\boldsymbol{\sigma}}(\mathbf{u}_h)$ and $\boldsymbol{\sigma}(\mathbf{u}_h)$. The most popular flux recovery method is the Zienkiewicz-Zhu Zienkiewicz and Zhu (1992a,b), which locally projects $\boldsymbol{\sigma}(\mathbf{u}_h)$ onto a higher-order polynomial approximation space over a patch of neighboring elements. Its popularity is due to its easy implementation, generality and accuracy. However, it is well known that adaptive mesh refinement algorithms using this estimator are not effective for interface problems, e.g. such as those encountered in topology optimization problems Ovall (2006); Cai et al (2017). This is because the tangential components of the stress field $\mathbf{t} \cdot \boldsymbol{\sigma}\mathbf{t}$, where $\mathbf{t}$ is any vector perpendicular to the interface normal vector, are discontinuous at the interface. Smoothing these components results in unnecessary overrefinement. Knowing that the stress field exists in the $H(\mathrm{div}, D) = \{v \in L^2(D, \mathbb{R}^n) : \mathrm{div}\ v \in L^2(D)\}$ space, Cai et al (2017) projects the stress field onto finite elements in this space. However, we do not follow this approach because $H(\mathrm{div}, D)$ finite elements are notoriously difficult to implement, especially in parallel computing environments.

Based on all these considerations, we use explicit residual-based a posteriori error estimates and follow Verfürth (1999) wherein the element error indicator for an element $K \in \mathcal{T}_h$, where $\mathcal{T}_h$ is the finite element mesh, is

$$\eta_K = \{h_K^2 \left\|\nabla \cdot \boldsymbol{\sigma}(\mathbf{u}_h) + \mathbf{f}\right\|^2_{L^2(K)} + \frac{1}{2} \sum_{E \in \mathcal{E}(K)} h_E \left\|j(\boldsymbol{\sigma}(\mathbf{u}_h) \cdot \mathbf{n})\right\|^2_{L^2(E)}\}^{1/2} . \tag{36}$$

In the above, the stress field is computed as

$$\boldsymbol{\sigma}(\mathbf{u}_h) = r(\tilde{\nu})\mathbb{C}[\nabla \mathbf{u}_h] \tag{37}$$

and

$$j(\boldsymbol{\sigma} \cdot \mathbf{n})_E = \begin{cases} [\![\boldsymbol{\sigma}(\mathbf{u}_h) \cdot \mathbf{n}]\!] & E \notin \mathcal{E}_D, \mathcal{E}_N \\ \mathbf{t}_N - \boldsymbol{\sigma}(\mathbf{u}_h) \cdot \mathbf{n} & E \in \mathcal{E}_N \end{cases} \tag{38}$$

is the traction jump across the element face E, which belongs to the set of faces of element K, $\mathcal{E}(K)$. $\mathcal{E}_D \subset \Gamma_D$ is the set of element faces with prescribed Dirichlet boundary condition and $\mathcal{E}_N \subset \Gamma_N$ is the set of element faces with prescribed $\mathbf{t}_N$ Neumann boundary condition. h_K is the element volume and h_E is the element face area.

Summing the element error η_K gives the global error

$$\eta = \left(\sum_{K \in \mathcal{T}_h} \eta_K^2 \right)^{1/2} . \tag{39}$$

This in turn is used to compute upper and lower bounds on the energy norm of the error, i.e.

$$|||\mathbf{u} - \mathbf{u}_h||| = \int_D r(\hat{\nu})\mathbb{C}[\nabla(\mathbf{u} - \mathbf{u}_h)] \cdot \nabla(\mathbf{u} - \mathbf{u}_h)\ \mathrm{d}V . \tag{40}$$

The upper bound $C\eta$ where C is a constant ensures that the error estimate is conservative, i.e.

$$|||\mathbf{u} - \mathbf{u}_h||| \leq C\eta . \tag{41}$$

On the other hand, the lower bound $c\eta$, where c is also a constant, ensures the error estimate is not excessively conservative, i.e.

$$c\eta \leq |||\mathbf{u} - \mathbf{u}_h||| . \tag{42}$$

To refine the mesh, we use the element error indicator η_K, cf. Equation (36). Refinement (coarsening) is done in those elements whose error is above the 70-th percentile (below the 5-th percentile) of the error indicator distribution.

Conventional error estimates are based on global measures such as the energy norm as in Equation (40) or the L^2-norm $\|\mathbf{u} - \mathbf{u}_h\|_{L^2}$. However these measures are not effective as we are only interested in accuracy of our optimization cost and constraint functions. For this purpose, goal-oriented error estimates were developed Oden and Prudhomme (2001); Becker and Rannacher (2001). As alluded to above, these estimates require the solution of the adjoint problem, which within our optimization context we have already solved to obtain the sensitivities.

To present the goal estimate, we discretize $\mathbf{u}$, i.e. we now find $\mathbf{u}_h \in V_h$ such that

$$a(\mathbf{u}_h, \mathbf{v}_h) = L(\mathbf{v}_h) \text{ for all } \mathbf{v}_h \in V_h , \tag{43}$$

where V_h is the finite element discretization of the function space V. Substracting Equation (12) from this and noting that $V_h \subseteq V$ yields the Galerkin orthogonality condition.

$$a(\mathbf{u} - \mathbf{u}_h, \mathbf{v}_h) = 0\ \forall \mathbf{v}_h \in V_h , \tag{44}$$

i.e. the error $\mathbf{u} - \mathbf{u}_h$ is a-orthogonal to V_h.

We are interested in defining the error $\theta(\mathbf{u}) - \theta(\mathbf{u}_h)$ in a goal functional $\theta(\mathbf{u}) : V \to \mathbb{R}$, i.e. a cost or constraint function. We start by restating the adjoint problem in Equation (34). Dropping the argument ν for conciseness and replacing $\delta\mathbf{u}$ with $\mathbf{w}$ we find $\mathbf{v} \in V$ such that

$$a(\mathbf{v}, \mathbf{w}) = \delta_{\mathbf{u}}\theta(\mathbf{u}; \mathbf{w}) \text{ for all } \mathbf{w} \in V\,. \tag{45}$$

Expanding $\theta(\mathbf{u}) - \theta(\mathbf{u}_h)$ in first-order Taylor series and applying Equation (45) we find

$$\begin{aligned}
\theta(\mathbf{u}) - \theta(\mathbf{u}_h) &= \theta(\mathbf{u}) - \theta(\mathbf{u} + \mathbf{u}_h - \mathbf{u})\,, && (46)\\
&= \theta(\mathbf{u}) - \theta(\mathbf{u}) - \delta_{\mathbf{u}}\theta(\mathbf{u}; \mathbf{u}_h - \mathbf{u}) \\
&\qquad - o\left\|\mathbf{u}_h - \mathbf{u}\right\|^2\,, && (47)\\
&= \delta_{\mathbf{u}}\theta(\mathbf{u}; \mathbf{u}_h - \mathbf{u})\,, && (48)\\
&= a(\mathbf{v}, \mathbf{u} - \mathbf{u}_h)\,, && (49)\\
&= a(\mathbf{u} - \mathbf{u}_h, \mathbf{v})\,. && (50)
\end{aligned}$$

Equation (50) [1] gives us the error estimate for the quantity of interest θ, however, the exact adjoint solution $\mathbf{v}$ is unknown, rather we compute $\mathbf{v}_h$ using the discretization that is used to compute $\mathbf{u}_h$, but this yields a zero error estimate by Galerkin orthogonality of (44). A common technique to resolve this issue is to calculate $\mathbf{v}_h$ over a more refined mesh or to post-process $\mathbf{v}_h$ to obtain a higher order approximation. We instead follow Garg (2012) and add the zero Galerkin orthogonality Equation (44) to Equation (50) and apply Cauchy-Schwarz inequality to obtain bounds on the error.

$$\begin{aligned}
\theta(\mathbf{u}) - \theta(\mathbf{u}_h) &= a(\mathbf{u} - \mathbf{u}_h, \mathbf{v} - \mathbf{v}_h)\,, && (51)\\
&= \int_D r(\hat{\nu})\mathbb{C}[\nabla(\mathbf{u} - \mathbf{u}_h)] \\
&\qquad \cdot [\nabla(\mathbf{v} - \mathbf{v}_h)]\; dV\,, && (52)\\
&\leq \left\| \sqrt{r(\hat{\nu})\mathbb{C}}[\nabla(\mathbf{u} - \mathbf{u}_h)] \right\|_{L^2} \\
&\qquad \times \left\| \sqrt{r(\hat{\nu})\mathbb{C}}[\nabla(\mathbf{v} - \mathbf{v}_h)] \right\|_{L^2}\,, && (53)\\
&= |||\mathbf{u} - \mathbf{u}_h|||\,|||\mathbf{v} - \mathbf{v}_h|||\,. && (54)
\end{aligned}$$

With these bounds, we can reformulate the error estimate in terms of the energy norms:

$$\begin{aligned}
\theta(\mathbf{u}) - \theta(\mathbf{u}_h) &\leq |||\mathbf{u} - \mathbf{u}_h|||\,|||\mathbf{v} - \mathbf{v}_h|||\,, && (55)\\
&\leq \sum_{K \in \mathcal{T}_h} |||\mathbf{u} - \mathbf{u}_h|||_K\, |||\mathbf{v} - \mathbf{v}_h|||_K\,, && (56)\\
e_K &= |||\mathbf{u} - \mathbf{u}_h|||_K\, |||\mathbf{v} - \mathbf{v}_h|||_K\,. && (57)
\end{aligned}$$

The expression inside the summation is the K element error indicator Equation (57) which is used to mark cells for refinement and coarsening throughout the optimization. We compute the error indicator $|||\mathbf{u} - \mathbf{u}_h|||_K = \eta_K$ from Equations (36)–(37). The estimate for $|||\mathbf{v} - \mathbf{v}_h|||_K$ is similarly computed using Equations (36)–(37), but we replace $\mathbf{u}_h$ with $\mathbf{v}_h$ and $\mathbf{f}$ and $\mathbf{t}_N$ with their corresponding body load and traction from the adjoint linear term $\delta_{\mathbf{u}}\theta$. With the error indicator e_K for each element, we proceed as in the energy error approach and refine the elements whose error is above the 70-th percentile of the error indicators distribution and coarsen those below the 5th percentile. We only use the element error indicator (57) and not the goal estimate (56), as it is not accurate Garg (2012).

[1] In Equation (48), we have neglected the higher order terms. For details on higher order nonlinear functionals, we refer to Becker and Rannacher (2001).

4.2 Optimization algorithm and refinement strategy

Our optimization framework uses the C++ MMA Svanberg (1987) implementation by Aage et al (2015). We implement a continuation strategy for the β parameter in the threshold function Equation (9) and for the penalty parameter γ in Equation (26). We do not wait for MMA to converge to change these parameters, rather we increase them following a heuristic strategy.

For each optimization iteration k, we use the current design estimate ν_k to calculate the state $\mathbf{u}_h$ and adjoint $\mathbf{v}_h$ states, which are needed to calculate the cost θ_0 and constraint θ_i functions and their gradients $\nabla\theta_0$ and $\nabla\theta_i$ for $(i = 1, ..., n_i)$. These are fed into the optimizer which then updates the design to ν_{k+1}, cf. Algorithm 1. During each optimization iteration, we determine if the relative change in the cost function between iterations is smaller than tol_{AMR}. If so, we invoke our AMR strategy described earlier. The MMA mesh dependent information, i.e. the design field and Lagrangian multiplier variables over the last three iterations Svanberg (1987), are interpolated onto the new mesh. Next, the filter kernel is reconstructed. We update the threshold and penalty parameters β and γ following a heuristic strategy explained in the numerical examples. Finally, tol_{AMR} is updated such that its value is halved after each refinement. We reset tol_{AMR} to its starting value once the threshold parameter β exceeds 200 so as to reinitiate the refinement. The termination criteria for the optimization is based on the change in the design or the maximum number of iterations, set to 500.

4.3 Finite Element Implementation

The finite element computations are performed in parallel thanks to the libMesh finite element library Kirk et al (2006). For solvers we use PETSc Balay et al

Algorithm 1 Algorithm outline.

Build filter.
while $\|\nu_k - \nu_{k+1}\| > tol$ or $it < maxit$ **do**
  Solve state problem to obtain $\mathbf{u}$
  Solve adjoint problem to obtain $\mathbf{v}$
  Calculate $\theta_0(\nu_k)$, $\nabla\theta_0(\nu_k)$
  Update ν_{k+1} according to the MMA algorithm.
  if $\frac{\theta_0(\nu_k)-\theta_0(\nu_{k+1})}{\theta_0(\nu)} \leq tol_{AMR}$ **then**
    Calculate η_K for $K = 1...nel$
    Sort element errors in decreasing order.
    Refine of 30 % of the elements with highest errors.
    Coarsen of 5 % of the elements with lowest errors.
    Update filter with the new mesh.
    Project MMA data into the new discretization.
    Update tol_{AMR}
  end if
  if β satisfies β-criteria **then**
    Update β
  end if
  if γ satisfies γ-criteria **then**
    Update γ
  end if
end while

(1997, 2016), and the HYPRE LLNL (2018) preconditioner. As both the adjoint and primal problems share the same stiffness matrix, we recycle the preconditioner to avoid the overhead of multiple builds. libMesh uses a quadtree/octree data structure in their adaptive mesh refinement implementation. We use bilinear Lagrangian elements and accomodate the hanging nodes via constraint equations. Our code design is similar to that in Garg (2012) wherein the users need only write the optimization cost and constraint functions and their derivatives with respect to $\mathbf{u}$ and ν. All the optimizations were run on a 8-core 2.60 GHz Intel Xeon E5-2670 processor.

4.4 Numerical examples

We first benchmark our algorithm with the eyebar example from Amstutz and Novotny (2010). The design domain in Figure 11 is discretized with the Gmsh library Christophe and Jean-Franois (2009) using second order triangles to capture the circumference with more precision and avoid sharp angles when refining the mesh. The largest triangle has an inradius of 0.15 mm and the smallest, 0.10 mm, placed near the hole. The load applied on the left hand side of the hole follows the distribution $\mathbf{t}(x, y) = (-((y-4)^2 - 1.5^2), 0.0)$ and Dirichlet boundary conditions are applied to the 2 mm segment in the right side. The isotropic material has a Young's modulus $E = 1.0$ MPa, a Poisson's ratio of $\nu = 0.3$ and a yield criteria is $\sigma_y = 5\ MPa$. The filter radius is $\epsilon = 0.6\ mm$. The initial mesh contains 681 elements. We limit the maximum refinement level to four because the relatively large filter radius compared to the mesh dimensions causes the filter kernel to exhaust the computer's memory if the refinement is too high.

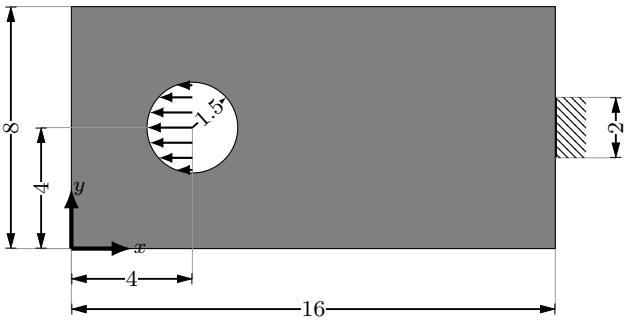

Fig. 11 Gray design domain, loads and boundary conditions. All dimensions are in mm.

Our continuation strategy to obtain optimized designs is as follows. First, the threshold parameter β starts with a value of 1 and is increased by 5 every 20 iterations after iteration 50 to avoid having the design fall into a local minimum. Second, the penalty parameter γ starts with a value of 10 and is increased by 50 every 50 iterations after iteration 50. The tolerance to trigger refinement tol_{AMR} is 1e-2.

We plot the optimized design in Figure 12. As we can see, part of the structure is stuck to the right side of the hole. The reason being that, thanks to the threshold function of Equation (9), the sensitivities are only significant in the material-void transition regions, i.e. at the design boundaries. If the hold-all domain boundary ∂D coincides with the intended design domain boundary, it is difficult to move the latter, as the sensitivity is zero there because the design boundary interface cannot fully resolve itself. For this reason we expand the domain into the hole, cf. Figure 13. To recover the intended design domain, we impose a zero volume constraint for the thresholded volume fractions $\tilde{\nu}$ in the extended, i.e. red, region.

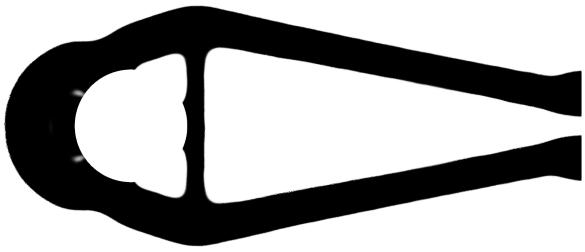

Fig. 12 Optimized design for the eyebar geometry.

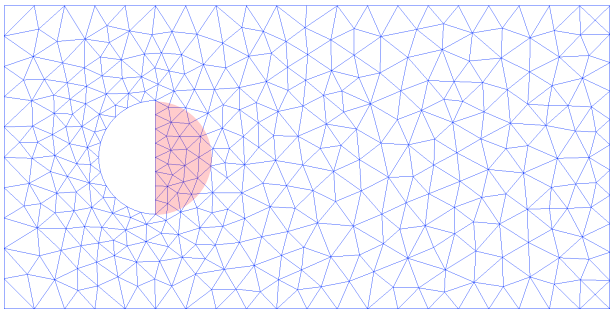

Fig. 13 Initial mesh with extended simulation domain in red.

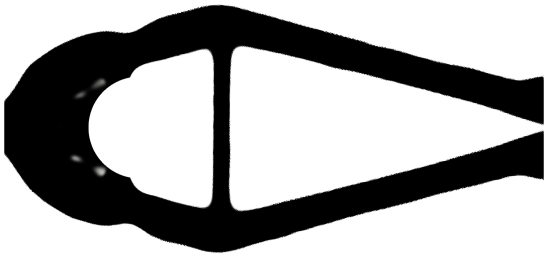

Fig. 14 Optimized design with a zero volume constraint in the extended region.

We plot the new design in Figure 14. The nonlocal nature of the filter causes the zero volume constraint to extend its influence beyond the actual hole. To resolve this, in the extended domain, we equate $\nu = 0$ and $\epsilon = 0$ to avoid nonzero filtered volume fractions within the hole.

We first run an optimization using the global energy norm error indicator described in Section 4.1. The result with this approach cf. Figure 15, shows how the algorithm fails to obtain a complete 0/1 design. Indeed, the lack of a global convergence mechanism in MMA causes an oscillatory behavior in the boundary region near the hole. We also plot the Von Mises Stress field in Figure 16. The optimization time was 1900.8 seconds, out of which 339.5 seconds were devoted to the filter kernel construction.

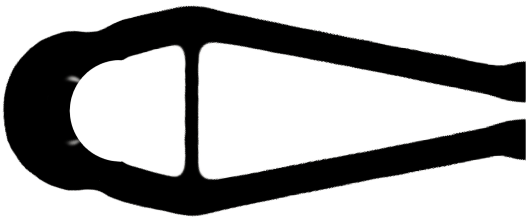

Fig. 15 Optimized design for the eyebar geometry with the global energy error indicator and $\nu = 0$ and $\epsilon = 0$ in the extended simulation domain.

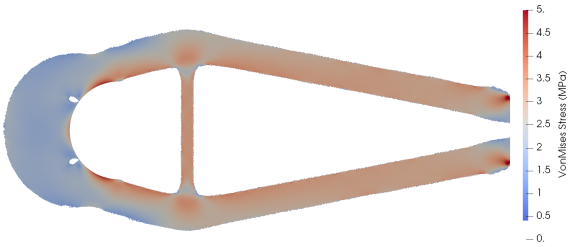

Fig. 16 Von Mises stress field for the eyebar design in Figure 15.

Using the same parameters as the previous case, we run an optimization using the goal-oriented error indicator with respect to the cost function, cf. Equation (25). The new optimized design in Figure 17 is almost identical to that obtained with the global energy error indicator, cf. Figure 15. The optimization took 1893.6 seconds, with 313.91 devoted to the filter kernel. The evolution of the cost function is similar as well, but the refinement process is not, cf. Figure 18. The goal error indicator initially refines fewer elements than the energy error where after it refines more until the difference stagnates due to the ceiling on the maximum level of refinement. The upticks in the value of the cost function correspond to mesh refinements, which resulted in higher stress values.

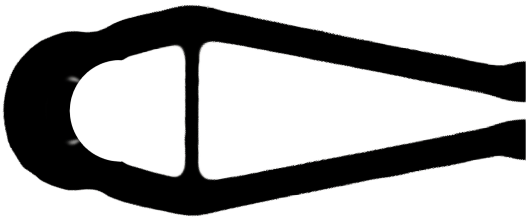

Fig. 17 Optimized design for the eyebar geometry with the goal-oriented error indicator and $\nu = 0$ and $\epsilon = 0$ in the extended simulation domain.

For the sake of comparison, we study the "L-bracket" problem described in Le et al (2010), cf. Figure 19. We apply 0.08 N/mm traction over the load region, the isotropic material model has again a Youngs modulus of $E = 1.0$ MPa , Poissons ratio of $\nu = 0.3$ and $\epsilon_\nu = 10^{-4}$; the filter radius is $\epsilon = 2.0$ mm and the maximum allowable Von Mises stress is $\sigma_y = 2$ MPa. The initial design uses the mesh in Figure 20 which defines refinement level 0.

Again, there are several knobs that need to be adjusted to obtain the optimized design. First, the thresh-

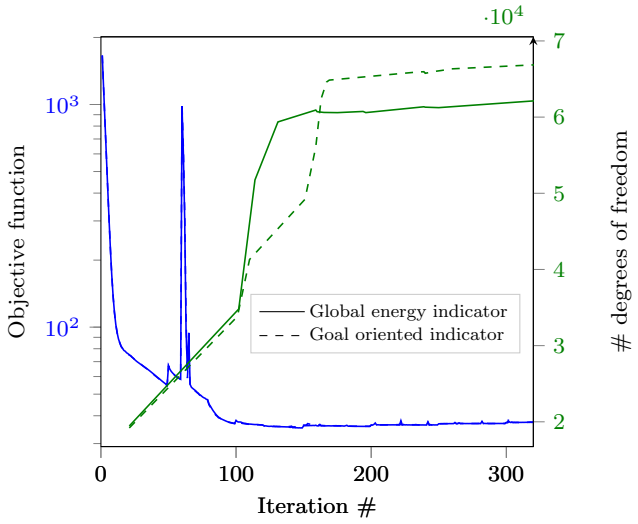

Fig. 18 Cost function and discretization degrees of freedom histories for the eyebar.

old parameter β in Equation (9) starts with a value of 1 and is not increased until iteration number 100. Thereafter then increased by 5 every 20 iterations up to a maximum value of 250. This is necessary to obtain a sharp interface and also prevents the design from falling into local minima. Second, the penalty parameter γ starts with an initial value of 1 and increases by 2 every 20 iterations after iteration 50. Third, the maximum refinement level is fixed at 3 until iteration 200, 5 until iteration 400, and 8 thereafter. These strategies give us the best results. For example, it prevents areas with intermediate volume fraction values from being overly refined given that they are eliminated with the threshold function later in the optimization.

The tolerance to trigger the refinement tol_{AMR} is initially 1e-2; it is halved after each refinement. As such tol_{AMR} can become very small early in the design process, i.e. while the primary topology is still evolving. This is attributed to the threshold function, which makes the problem similar to a shape optimization. Therefore, we reset tol_{AMR} =1e-2 every 80 iterations after iteration 100.

As in the previous example, we extend the simulation domain beyond the design domain, cf. the red region in Figure 20. We likewise equate $\nu = 0$ and $\epsilon = 0$ in these red areas. This approach however, does not work well for the L-bracket problem. As seen in Figure 21, there is still part of the material stuck at the L-bracket corner. The corner creates a high stress concentration, but the gradient is zero there due to the threshold operation in (9), as explained earlier. For this reason, we revert to our previous approach and place a zero constraint on thresholded volume fractions $\tilde{\nu}$ in the extended region; we no longer have $\nu = 0$ and $\epsilon = 0$. As in Figure 20 design, we run an optimization using the global energy norm error indicator described in Section 4.1. Our result in Figure 22 shows an optimized design with a volume of 1228.49 mm^2. The final mesh contains 524,842 elements. The same mesh with a uniform refinement corresponding to the smallest element would contain 6,160,384 elements.

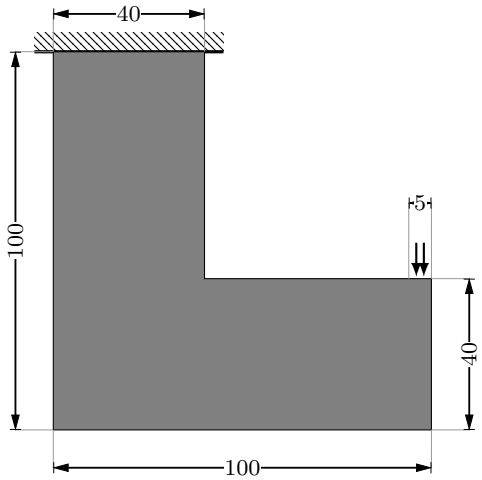

Fig. 19 Gray design domain, loads and boundary conditions.. All dimensions are in mm.

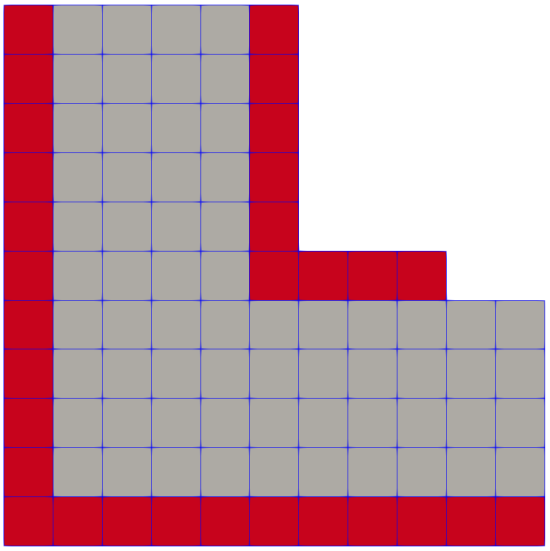

Fig. 20 Initial mesh for the optimization and actual design domain shown in gray. A zero volume constraint is imposed in the extended domain shown in red.

We plot the Von Mises stress distribution calculated using the SIMP stress formula given in the weak form

in Equation (14), i.e. $\boldsymbol{\sigma} = r(\tilde{\nu})\mathbb{C}[\nabla \mathbf{u}]$, cf. Figure 23. The distribution is considerably more uniform, which indicates a more optimized design. We plot the mesh corresponding to the optimized design with different zoom levels in Figure 26. Note the high refinement level that it is necessary to accurately compute the stress field.

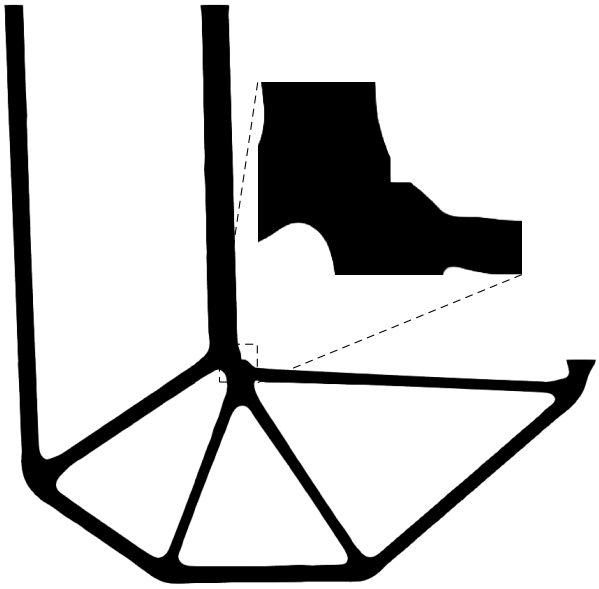

Fig. 21 Optimized design using $\nu = 0$ and $\epsilon = 0$ in the extended region.

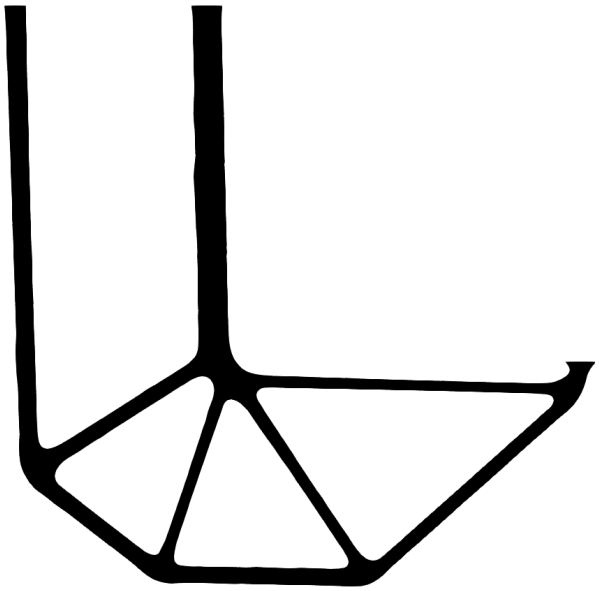

Fig. 22 Optimized design using zero volume constraint on the thresholded volume fractions in the extended region.

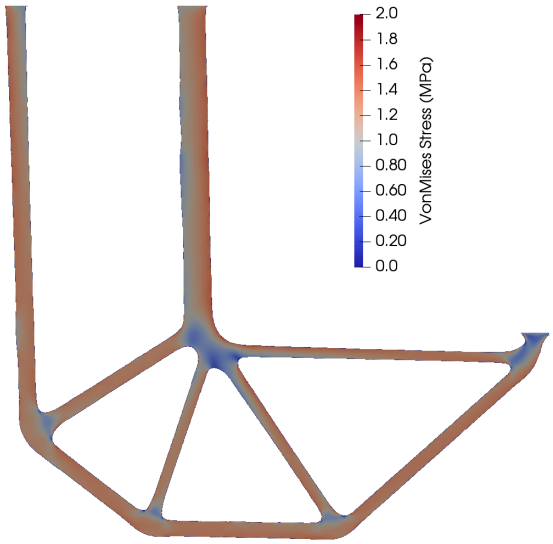

Fig. 23 Von Mises stress for the design of Figure 22.

The total computational cost was of 2181.6 seconds. Out of this time, 797.2 seconds were devoted on building the cone filter in Equation (7). This expensive operation is done every time the mesh is refined and has an algorithmic complexity that is polynomial with respect to the number of elements. Based on this, it is even more compeling to find out a way to use Lazarov and Sigmund (2011) in the context of AMR.

Using the same parameters as the previous case, we run another optimization but we replace the global energy error indicator for the goal-oriented error indicator, cf. Equation (25) to obtain the best possible accuracy. The optimized design is similar than that obtained with the global energy error indicator, cf. Figures 22 and 24. The total volume is 1233.01 mm^2 and the mesh contains 516,346 elements which is less than those obtained via the global energy error indicator.

The goal-oriented optimization took 2120.4 seconds. Figure 25 shows the evolution of the cost function and the number of degrees of freedom for the displacement field. The goal oriented error indicator marks fewer elements for refinement than the energy error indicator which translates into a slight computational saving for our case. The global nature of the goal error, Equation (25), explains the similar number of elements versus the energy error. A cost function localized in a small region would have resulted in a more localized mesh refinement because the adjoint response would only be significant in the small region.

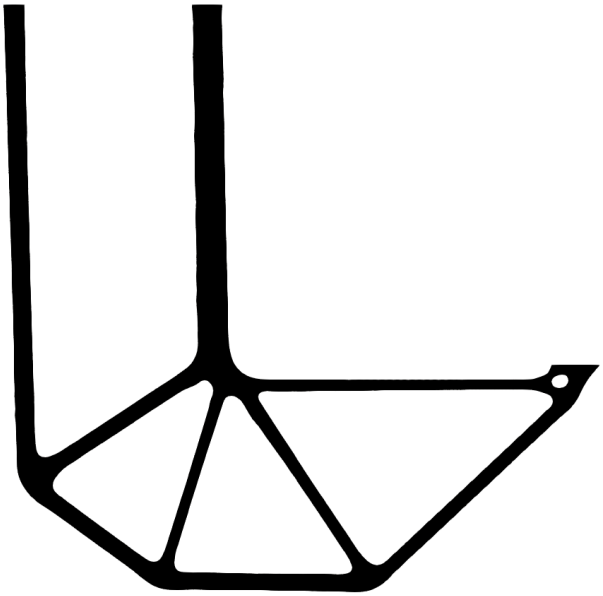

Fig. 24 Optimized design using the goal oriented error indicator.

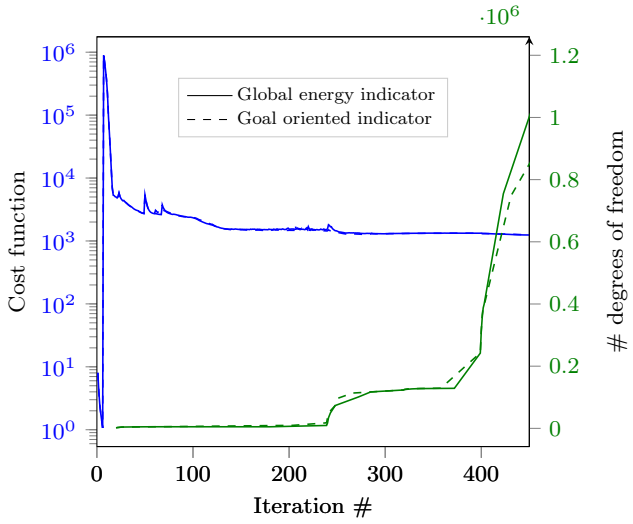

Fig. 25 Cost function and discretization degrees of freedom histories for the L-bracket.

4.5 Design validation with explicit geometry finite element simulation

To validate the Figure 22 design, we use the $\tilde{\nu} = 0.5$ level set of the thresholded volume fraction field to define the optimized geometry. A body-fitted mesh is genererated over this domain and a finite element analysis is performed to compute the displacement and stress fields using the finite element library FEniCS Alnæs et al (2015). We plot the difference between the fitted and topology optimized (topopt) Von Mises stress fields $\sigma_{VM}^{\text{fitted}} - \sigma_{VM}^{\text{topopt}}$, cf. Figure 27. As we can see, most of

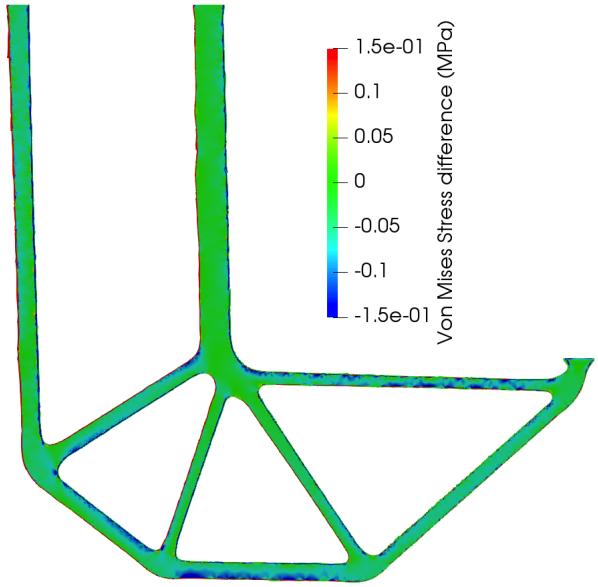

Fig. 27 Von Mises stress field verification.

the difference is within 10% of the maximum von mises stress value of 2 MPa, with $\sigma_{VM}^{\text{topopt}}$ slightly greater than $\sigma_{VM}^{\text{fitted}}$.

For comparison purposes, we run a similar optimization with a single uniform mesh containing 528,384 elements, which is similar to the number of elements in the optimal design of Figure 22. This result is plotted in Figure 28 with a total volume of 1381.9 mm^2. We perform a similar validation study with a body fitted mesh and plot the result in Figure 29, as expected the lack of refinement creates a greater difference in the Von Mises stress field over the design boundaries and in the thin structural members. Increasing the refinement with two additional levels to match the most refined elements in our AMR mesh will improve the stress field, but this uniform mesh would result in 8,454,144 elements, versus the 524,842 elements in our AMR mesh.

5 Conclusion and future work

We presented a new topology optimization methodology to obtain designs in structural mechanics with accurate stress fields that satisfy yield criteria. We are able to do so by combining a threshold function that sharpens the otherwise blurred boundaries from the filter operation and adaptive mesh refinement that increases the mesh resolution in the boundary region. We validated the stress accuracy by using geometries whose stress fields are known and tabulated. The eye-bar and L-bracket example problems are used to validate our approach. We foresee that it is possible to further im-

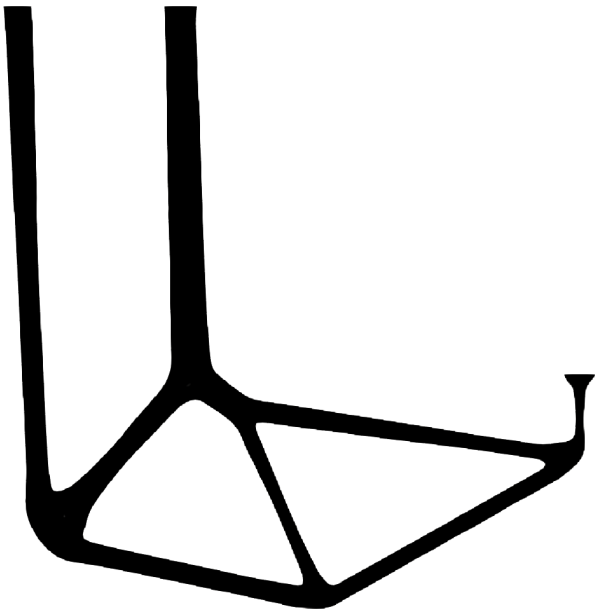

Fig. 28 Optimized design with a uniform mesh.

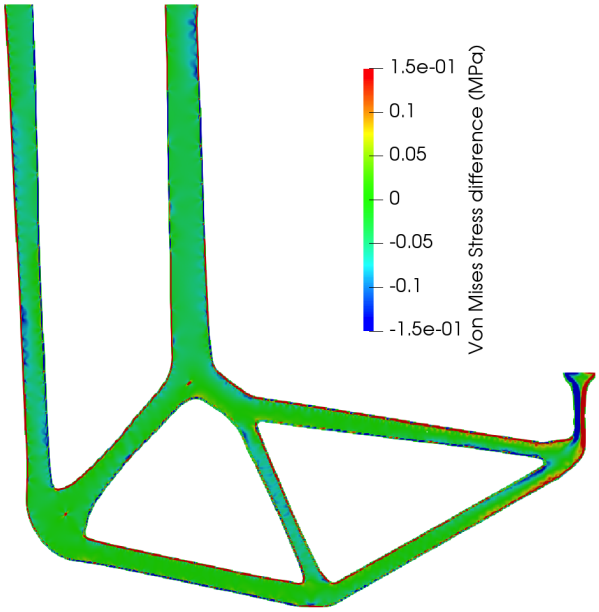

Fig. 29 Von Mises stress field difference for the optimized design with $\sigma_y = 2$ MPa and a uniform mesh

prove our results by using a globally convergence optimization algorithm such as the GCMMA Svanberg (2002) and the PDE-based filter Lazarov and Sigmund (2011) to reduce memory requirements.

Future work will address a more rigurous mesh refinement strategies. One that considers the inexactness of the finite element approximation and still ensures global convergence to a local minima Ziems and Ulbrich (2011). This will avoid our current heuristic and case dependent strategy, e.g. for the assignment of β, tol_{AMR}, etc. Indeed for this approach to be succesful, it is necessary to employ error estimates and error indicators with tighter bounds than the currently used residual based approaches. To save computational resources, uncoupling the discretizations of the volume fraction field and the displacement field could be incorporated.

6 Acknowledgements

This work was performed under the auspices of the U.S. Department of Energy by Lawrence Livermore National Laboratory under Contract DE-AC52-07NA27344. The author thanks the Livermore Graduate Scholar Program for its support.

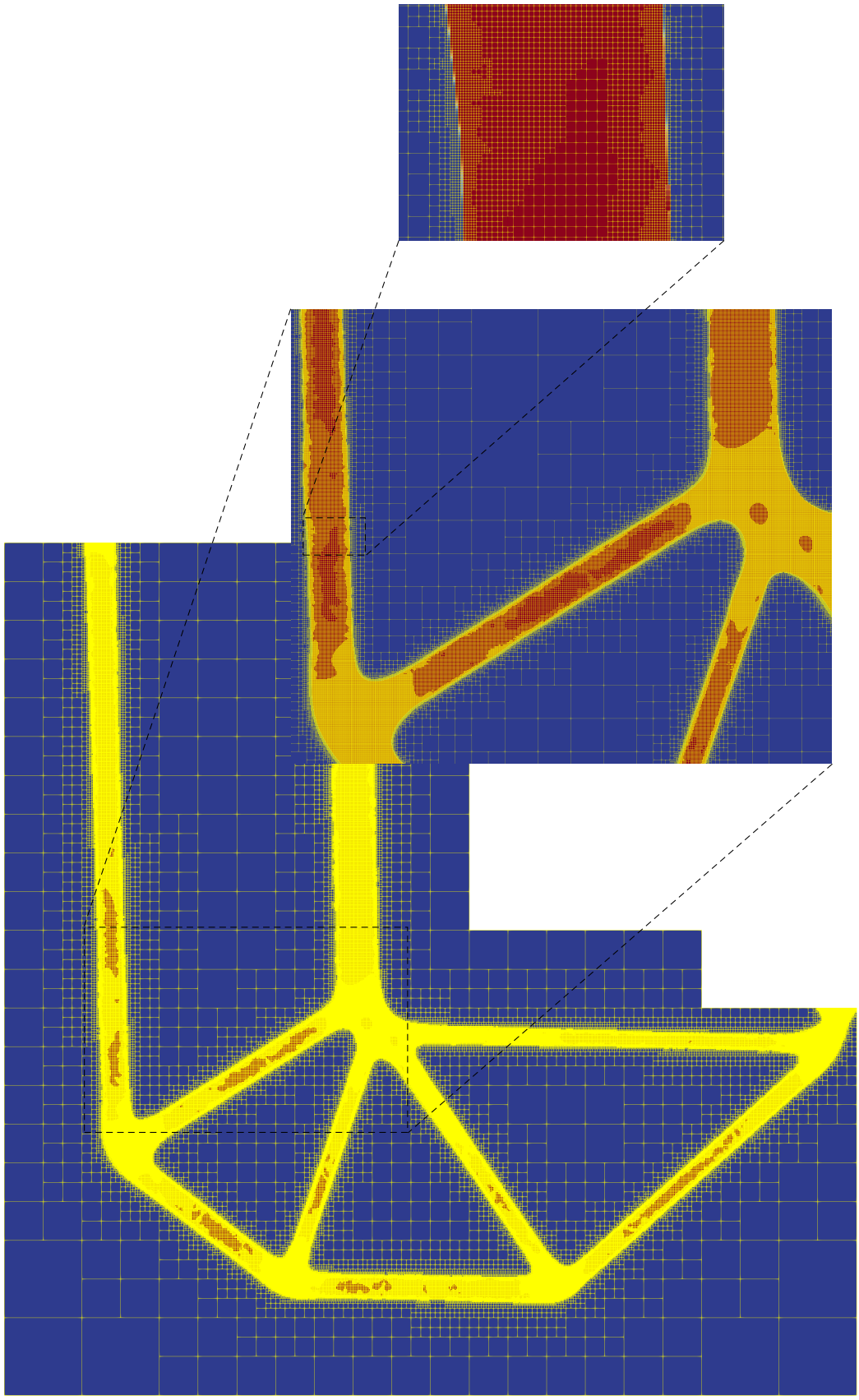

Fig. 26 Final mesh for the design in Figure 22.

References

Aage N, Andreassen E, Lazarov BS (2015) Topology optimization using petsc: An easy-to-use, fully parallel, open source topology optimization framework. Structural and Multidisciplinary Optimization 51(3):565–572

Ainsworth M, Oden JT (2011) A posteriori error estimation in finite element analysis, vol 37. John Wiley & Sons

Allaire G, Dapogny C, Frey P (2014) Shape optimization with a level set based mesh evolution method. Computer Methods in Applied Mechanics and Engineering p doi:10.1016/j.cma.2014.08.028, URL http://hal.upmc.fr/hal-00933545

Alnæs MS, Blechta J, Hake J, Johansson A, Kehlet B, Logg A, Richardson C, Ring J, Rognes ME, Wells GN (2015) The fenics project version 1.5. Archive of Numerical Software 3(100), DOI 10.11588/ans.2015.100.20553

Amstutz S, Novotny AA (2010) Topological optimization of structures subject to von mises stress constraints. Structural and Multidisciplinary Optimization 41(3):407–420, DOI 10.1007/s00158-009-0425-x, URL https://doi.org/10.1007/s00158-009-0425-x

Balay S, Gropp WD, McInnes LC, Smith BF (1997) Efficient management of parallelism in object oriented numerical software libraries. In: Arge E, Bruaset AM, Langtangen HP (eds) Modern Software Tools in Scientific Computing, Birkhäuser Press, pp 163–202

Balay S, Abhyankar S, Adams MF, Brown J, Brune P, Buschelman K, Dalcin L, Eijkhout V, Gropp WD, Kaushik D, Knepley MG, McInnes LC, Rupp K, Smith BF, Zampini S, Zhang H, Zhang H (2016) PETSc users manual. Tech. Rep. ANL-95/11 - Revision 3.7, Argonne National Laboratory

Becker R, Rannacher R (2001) An optimal control approach to a posteriori error estimation in finite element methods. Acta numerica 10:1–102

Bendsøe MP, Sigmund O (1999) Material interpolation schemes in topology optimization. Archive of Applied Mechanics 69(9):635–654, DOI 10.1007/s004190050248, URL https://doi.org/10.1007/s004190050248

Bourdin B (2001) Filters in topology optimization. International Journal for Numerical Methods in Engineering 50(9):2143–2158, DOI 10.1002/nme.116, URL http://dx.doi.org/10.1002/nme.116

Bruggi M (2008) On an alternative approach to stress constraints relaxation in topology optimization. Structural and multidisciplinary optimization 36(2):125–141

Bruggi M, Verani M (2011) A fully adaptive topology optimization algorithm with goal-oriented error control. Computers & Structures 89(15):1481 – 1493, DOI http://dx.doi.org/10.1016/j.compstruc.2011.05.003, URL http://www.sciencedirect.com/science/article/pii/S0045794911001337

Bruns TE, Tortorelli DA (2001) Topology optimization of non-linear elastic structures and compliant mechanisms. Computer Methods in Applied Mechanics and Engineering 190(26):3443 – 3459, DOI http://dx.doi.org/10.1016/S0045-7825(00)00278-4, URL http://www.sciencedirect.com/science/article/pii/S0045782500002784

Cai Z, He C, Zhang S (2017) Improved {ZZ} a posteriori error estimators for diffusion problems: Conforming linear elements. Computer Methods in Applied Mechanics and Engineering 313:433 – 449, DOI https://doi.org/10.1016/j.cma.2016.10.006, URL http://www.sciencedirect.com/science/article/pii/S0045782516302183

Cheng G, Guo X (1995) A note on star shape feasible domain in structural topology optimization. In: Proceedings of the Second China-Japan Symposium on Optimization of Structural and Mechanical Systems, Beijiag

Cheng G, Guo X (1997) ε-relaxed approach in structural topology optimization. Structural and Multidisciplinary Optimization 13(4):258–266

Cheng G, Jiang Z (1992) Study on topology optimization with stress constraints. Engineering Optimization 20(2):129–148

Christophe G, Jean-Franois R (2009) Gmsh: A 3-d finite element mesh generator with built-in pre- and post-processing facilities. International Journal for Numerical Methods in Engineering 79(11):1309–1331, DOI 10.1002/nme.2579, URL https://onlinelibrary.wiley.com/doi/abs/10.1002/nme.2579, https://onlinelibrary.wiley.com/doi/pdf/10.1002/nme.2579

Costa Jr JCA, Alves MK, Al-Qureshi HA (2005) A stress based h-adaptive topology optimization method. Proceedings of COBEM 2005 : 18th international congress of mechanical engineering

De Leon DM, Alexandersen J, O Fonseca JS, Sigmund O (2015) Stress-constrained topology optimization for compliant mechanism design. Structural and Multidisciplinary Optimization 52(5):929–943, DOI 10.1007/s00158-015-1279-z, URL https://doi.org/10.1007/s00158-015-1279-z

Dörfler W (1996) A convergent adaptive algorithm for poissons equation. SIAM Journal on Numerical Analysis 33(3):1106–1124, DOI 10.1137/0733054, URL https://doi.org/10.1137/0733054, https://doi.org/10.1137/0733054

Duysinx P, Bendsøe MP (1998) Topology optimization of continuum structures with local stress constraints. International journal for numerical methods in engineering 43(8):1453–1478

Gain AL, Paulino GH (2013) A critical comparative assessment of differential equation-driven methods for structural topology optimization. Structural and Multidisciplinary Optimization 48(4):685–710, DOI 10.1007/s00158-013-0935-4, URL https://doi.org/10.1007/s00158-013-0935-4

Garg VV (2012) Coupled flow systems, adjoint techniques and uncertainty quantification. PhD thesis, The University of Texas at Austin

Guilherme CEM, Fonseca JSO (2007) Topology optimization of continuum structures with epsilon-relaxed stress constraints. International Symposium on Solid Mechanics (2007 mar 05-07 : So Paulo, SP)

Guo X, Zhang WS, Wang MY, Wei P (2011) Stress-related topology optimization via level set approach. Computer Methods in Applied Mechanics and Engineering 200(47):3439 – 3452, DOI http://dx.doi.org/10.1016/j.cma.2011.08.016, URL http://www.sciencedirect.com/science/article/pii/S0045782511002714

Guo X, Zhang W, Zhong W (2014) Stress-related topology optimization of continuum structures involving multi-phase materials. Computer Methods in Applied Mechanics and Engineering 268:632 – 655, DOI http://dx.doi.org/10.1016/j.cma.2013.10.003, URL http://www.sciencedirect.com/science/article/pii/S0045782513002557

Haber RB, Jog CS, Bendsøe MP (1996) A new approach to variable-topology shape design using a constraint on perimeter. Structural and Multidisciplinary Optimization 11(1):1–12

Hintermüller M, Hinze M (2009) Moreau-Yosida regularization in state constrained elliptic control problems: Error estimates and parameter adjustment. SIAM Journal on Numerical Analysis 47(3):1666–1683, DOI 10.1137/080718735, URL https://doi.org/10.1137/080718735, https://doi.org/10.1137/080718735

Holmberg E, Torstenfelt B, Klarbring A (2013) Stress constrained topology optimization. Structural and Multidisciplinary Optimization 48(1):33–47, DOI 10.1007/s00158-012-0880-7, URL https://doi.org/10.1007/s00158-012-0880-7

Jensen KE (2016) Solving stress and compliance constrained volume minimization using anisotropic mesh adaptation, the method of moving asymptotes and a global p-norm. Structural and Multidisciplinary Optimization 54(4):831–841

Kirk BS, Peterson JW, Stogner RH, Carey GF (2006) libMesh: A C++ Library for Parallel Adaptive Mesh Refinement/Coarsening Simulations. Engineering with Computers 22(3–4):237–254, URL https://doi.org/10.1007/s00366-006-0049-3

Kirsch U (1990) On singular topologies in optimum structural design. Structural optimization 2(3):133–142

Lazarov BS, Sigmund O (2011) Filters in topology optimization based on helmholtz-type differential equations. International Journal for Numerical Methods in Engineering 86(6):765–781, DOI 10.1002/nme.3072, URL http://dx.doi.org/10.1002/nme.3072

Le C, Norato J, Bruns T, Ha C, Tortorelli D (2010) Stress-based topology optimization for continua. Structural and Multidisciplinary Optimization 41(4):605–620, DOI 10.1007/s00158-009-0440-y, URL https://doi.org/10.1007/s00158-009-0440-y

Lian H, Christiansen AN, Tortorelli DA, Sigmund O, Aage N (2017) Combined shape and topology optimization for minimization of maximal von mises stress. Structural and Multidisciplinary Optimization 55(5):1541–1557, DOI 10.1007/s00158-017-1656-x, URL https://doi.org/10.1007/s00158-017-1656-x

LLNL (2018) *hypre*: High Performance Preconditioners. Lawrence Livermore National Laboratory, URL http://www.llnl.gov/CASC/hypre/

Maute K, Ramm E (1995) Adaptive topology optimization. Structural optimization 10(2):100–112, DOI 10.1007/BF01743537, URL https://doi.org/10.1007/BF01743537

Nana A, Cuillière JC, Francois V (2016) Towards adaptive topology optimization. Advances in Engineering Software 100:290–307

Nguyen-Xuan H (2017) A polytree-based adaptive polygonal finite element method for topology optimization. International Journal for Numerical Methods in Engineering 110(10):972–1000, DOI 10.1002/nme.5448, URL http://dx.doi.org/10.1002/nme.5448, nme.5448

Oden JT, Prudhomme S (2001) Goal-oriented error estimation and adaptivity for the finite element method. Computers & mathematics with applications 41(5-6):735–756

Ovall J (2006) The dangers to avoid when using gradient recovery methods for finite element error estimation and adaptivity. Tech. rep., Technical Report 6, Max Planck Institute for Mathematics in the Sciences

Panesar A, Brackett D, Ashcroft I, Wildman R, Hague R (2017) Hierarchical remeshing strategies with mesh mapping for topology optimisation. International Journal for Numerical Methods in Engineering 111(7):676–700, DOI 10.1002/nme.5488, URL http://dx.doi.org/10.1002/nme.5488, nme.5488

París J, Navarrina F, Colominas I, Casteleiro M (2010) Improvements in the treatment of stress constraints in structural topology optimization problems. Journal of computational and applied mathematics 234(7):2231–2238

Park YK (1995) Extensions of optimal layout design using the homogenization method. PhD thesis, University of Michigan

Petersson J, Sigmund O (1998) Slope constrained topology optimization. International Journal for Numerical Methods in Engineering 41(8):1417–1434, DOI 10.1002/(SICI)1097-0207(19980430)41:8⟨1417::AID-NME344⟩3.0.CO;2-N, URL http://dx.doi.org/10.1002/(SICI)1097-0207(19980430)41:8<1417::AID-NME344>3.0.CO;2-N

Rozvany G, Birker T (1994) On singular topologies in exact layout optimization. Structural and Multidisciplinary Optimization 8(4):228–235

Sharma A, Maute K (2018) Stress-based topology optimization using spatial gradient stabilized XFEM. Structural and Multidisciplinary Optimization 57(1):17–38, DOI 10.1007/s00158-017-1833-y, URL https://doi.org/10.1007/s00158-017-1833-y

Stainko R (2006) An adaptive multilevel approach to the minimal compliance problem in topology optimization. Communications in Numerical Methods in Engineering 22(2):109–118, DOI 10.1002/cnm.800, URL http://dx.doi.org/10.1002/cnm.800

Stolpe M, Svanberg K (2001) An alternative interpolation scheme for minimum compliance topology optimization. Structural and Multidisciplinary Optimization 22(2):116–124, DOI 10.1007/s001580100129, URL https://doi.org/10.1007/s001580100129

Svanberg K (1987) The method of moving asymptotesa new method for structural optimization. International journal for numerical methods in engineering 24(2):359–373

Svanberg K (2002) A class of globally convergent optimization methods based on conservative convex separable approximations. SIAM Journal on Optimization 12(2):555–573, DOI 10.1137/S1052623499362822, URL https://doi.org/10.1137/S1052623499362822, https://doi.org/10.1137/S1052623499362822

Svärd H (2015) Interior value extrapolation: a new method for stress evaluation during topology optimization. Structural and Multidisciplinary Optimization 51(3):613–629, DOI 10.1007/s00158-014-1171-2, URL https://doi.org/10.1007/s00158-014-1171-2

Sved G, Ginos Z (1968) Structural optimization under multiple loading. International Journal of Mechanical Sciences 10(10):803–805

Verfürth R (1999) A review of a posteriori error estimation techniques for elasticity problems. Computer Methods in Applied Mechanics and Engineering 176(1-4):419–440

Verfürth R (2013) A posteriori error estimation techniques for finite element methods. Oxford University Press, Oxford, UK

Wallin M, Ristinmaa M, Askfelt H (2012) Optimal topologies derived from a phase-field method. Structural and Multidisciplinary Optimization 45(2):171–183, DOI 10.1007/s00158-011-0688-x, URL https://doi.org/10.1007/s00158-011-0688-x

Wang F, Lazarov BS, Sigmund O (2011) On projection methods, convergence and robust formulations in topology optimization. Structural and Multidisciplinary Optimization 43(6):767–784, DOI 10.1007/s00158-010-0602-y, URL https://doi.org/10.1007/s00158-010-0602-y

Wang S, de Sturler E, Paulino GH (2010) Dynamic adaptive mesh refinement for topology optimization. arXiv preprint arXiv:10094975

Wang Y, Kang Z, He Q (2014) Adaptive topology optimization with independent error control for separated displacement and density fields. Computers & Structures 135:50 – 61, DOI http://dx.doi.org/10.1016/j.compstruc.2014.01.008, URL http://www.sciencedirect.com/science/article/pii/S0045794914000194

Xia Q, Shi T, Liu S, Wang MY (2012) A level set solution to the stress-based structural shape and topology optimization. Computers & Structures 90:55 – 64, DOI http://dx.doi.org/10.1016/j.compstruc.2011.10.009, URL http://www.sciencedirect.com/science/article/pii/S0045794911002562

Yang R, Chen C (1996) Stress-based topology optimization. Structural optimization 12(2-3):98–105

Young WC, Budynas RG (2002) Roark's formulas for stress and strain, vol 7. McGraw-Hill New York

Zhang WS, Guo X, Wang MY, Wei P (2013) Optimal topology design of continuum structures with stress concentration alleviation via level set method. International Journal for Numerical Methods in Engineering 93(9):942–959, DOI 10.1002/nme.4416, URL http://dx.doi.org/10.1002/nme.4416

Ziems JC, Ulbrich S (2011) Adaptive multilevel inexact sqp methods for pde-constrained optimization. SIAM Journal on Optimization 21(1):1–40, DOI 10.1137/080743160, URL https://doi.org/10.1137/080743160, https://doi.org/10.1137/080743160

Zienkiewicz OC, Zhu JZ (1992a) The superconvergent patch recovery and a posteriori error estimates. part 1: The recovery technique. International Journal for Numerical Methods in Engineering 33(7):1331–1364

Zienkiewicz OC, Zhu JZ (1992b) The superconvergent patch recovery and a posteriori error estimates. part 2: Error estimates and adaptivity. International Journal for Numerical Methods in Engineering 33(7):1365–1382